Performance evaluation of Charpy impact tests to investigate and detect process defects of a Ni-based superalloy elaborated by laser powder bed fusion

A. Ty, M. Mokhtari, Y. Balcaen, A. Votié, J.-M. Cloué, J. Alexis

Available online at www.sciencedirect.com

jmr&t Journal of Materials Research and Technology

journal homepage: www.elsevier.com/locate/jmrt

Performance evaluation of Charpy impact tests to investigate and detect process defects of a Ni-based superalloy elaborated by laser powder bed fusion

A. Ty [a], M. Mokhtari [a], Y. Balcaen [a,*], A. Votié [b], J.-M. Cloué [c], J. Alexis [a]

[a] Laboratoire Génie de Production, Ecole Nationale D'Ingénieurs de Tarbes, Université de Toulouse, LGP, ENIT/INPT, 47 Av. D'Azereix, BP1629, 65016 Tarbes Cedex, France

[b] Freyssinet Aero Equipement SA, P.A des Massiès, 81800 Couffouleux, France

[c] Spinodal Conseil, 1301 Avenue de Toulouse, 31600 Seysses, France

ARTICLE INFO

Article history:
Received 6 January 2023
Accepted 6 July 2023
Available online 13 July 2023

Keywords:
Charpy impact test
Additive manufacturing
L-PBF process
Inconel 718
Mechanical properties
Microstructure

ABSTRACT

Additive manufacturing is a robust process for building complex parts with improved mechanical properties. However, if a problem occurs during manufacturing, the production batch will present microstructural defects that reduce the mechanical properties and reliability of the part. Part post-processing represents a significant production time and production cost. Therefore, it is necessary to find a fast, simple, cheap, and efficient test to check production batch quality. High deformation rate tests are promising. We performed the Charpy impact test with reduced-size samples to investigate a specific height where defects may be suspected or critical. Charpy impact test's ability to detect an intentionally introduced defect in a tested sample is studied, involving exploitation of force-displacement data recorded during the test on reduced-size samples. For a defect localized within the notch plane, the results show that reduced-size samples allow for detecting a localized defect. Resilience values are reduced by 10%, and the force-displacement curves show a divergence in the propagation regime. Defects shifted from the notch plane are also detected, but not more than 500 μm, allowing the detection of production batch break.

1. Introduction

Additive manufacturing offers new design possibilities [1,2]. Laser-Powder Bed Fusion (LPBF), also known as selective laser melting, is a powder-based additive manufacturing technique. It allows the production of fully functional three-dimensional parts from a computer aided-design model [3–5]. Nickel-based superalloys are commonly used because of their excellent corrosion resistance, high-temperature strength, and limited thermal expansion [6–9]. There are some issues with machining them because of their high strength at elevated temperatures, tool-workpiece chemical affinity, hard abrasive carbides in the microstructure, and fairly low thermal conductivity [10–12]. Therefore, the production of complex geometries with reasonable three-dimensional accuracy by LPBF is promising for many industrial sectors [8].

However, if the LPBF process parameters are not optimized or an incident occurs during production, the production batch

* Corresponding author.
E-mail address: yannick.balcaen@enit.fr (Y. Balcaen).

https://doi.org/10.1016/j.jmrt.2023.07.064

will exhibit microstructural defects such as porosity, unmelted powder, and spatters, reducing the mechanical properties and reliability of the parts. Several authors have focused their research on these defects and their formation. One of the origins of the pores is gas trapped in the melt pool. This gas can be trapped during the atomization of powder particles. These defects are relatively spherical with a micro or sub-micron size. Some open porosities are reported, and they are attributed to the rapid solidification of the melt pool and its limited ability to fill the adjacent regions initially occupied by the shielding gas [5,7]. They have an irregular shape and are some hundred micrometers scaled. Some elongated pores (around 100–300 μm) in the scanning direction and located at the boundaries between two layers (inter-track pores or lack of fusion) are also reported [5,13,14]. Pores due to the keyhole effect reach 200 μm diameter. In situ monitoring could be a solution to detect defects early in the manufacturing process, but it is not industrially available [15]. Post-processing parts such as support structures removal, general surface finishing, heat treatment, and functional surfaces machining represents a significant production time, and cost [16] and environmental footprint [17]. Therefore, it is necessary to find a fast, simple, cheap, and efficient test to check the quality of production batches. Previous studies show a weak influence of porosity on tensile tests, especially for vertical samples [18,19]. Other studies suggest that high-strain rate tests may be more suitable for defect detection [20,21]. Indeed, high strain rates dynamic compression tests of additive manufactured TA6V, an intentionally introduced defect, have shown that there is a linear relationship between force and pore volume fraction [20]. In addition, the authors claim in their review [21] that the results of high-strain-rate fatigue tests could be correlated with the type and size of discontinuities and inhomogeneities.

Among high-strain rate tests, Charpy impact tests are very sensitive to the brittleness of the Laves-phase by Schirra et al. [22]. However, while hardness [7,13,23–28]. and tensile behavior [4,23,24,29,30–33] are well documented, few impact tests on alloy 718 specimens obtained by LPBF have been reported throughout the literature [3,24,26,31,32,34]. Fracture energy or resilience values are given; however, force-displacement curves and their analysis are not presented. Moreover, the influence of specimen geometries and surface roughness has not been investigated. Therefore, a Charpy impact test may be particularly suitable for detecting LPBF-induced defects in build samples in the early stages of manufacturing processes. Performed on samples extracted from the build platform just after fabrication, with minimal machining, such a test could be a helpful "go/no-go" check for subsequent finishing steps (heat treatments, extraction, and machining).

In order to analyze as-built specimens by impact testing, we have investigated the surface conditions' influence. Indeed, residual tensile stresses have been reported near the surface and in overlapping regions between two adjacent laser scanning paths for as-built specimens [35–37]. On the other hand, barrel finishing could be a solution to reach surface finish requirements of 2 μm (Ra) on bearing surfaces (ASTM E23-18). Although, as reported by Lesyk et al. [35], compressive residual stresses of approximately. 200 MPa on the near-surface (100 μm below the surface) have been reported in the case of barrel-finished samples. However, the notch was machined after barrel finishing. So, the crack initiation at the notch tip may be influenced only by notch-cutting conditions, and the propagation regime in the core of the sample is expected to be weakly influenced by abovementioned surface modifications.

Accordingly, the current work was undertaken to extend the mechanical properties documentation of alloy 718 obtained by LPBF. The use of undersized samples enables them to be extracted at a specific height, where defects can be suspected or could be critical. Finally, the ability of the Charpy impact test to detect an intentionally introduced defect in a tested sample is studied, involving the exploitation of force-displacement data recorded during the test on reduced-size samples.

2. Materials and methods

2.1. *Materials and building parameters*

From Alloy 718 powders (composition in Table 1), Fusia Aeroadditive (Toulouse – France) produced LPBF specimens on a Concept Laser M2 system (GE additive). Manufacturing parameters are given in Table 2. Two production batches were built. The first aimed to determine the best conditions to perform the Charpy tests with three different surface finishes: as-built and barrel finishing with two different arithmetic mean roughness (Ra equal to 6.3 μm and 3.2 μm). The barrel finishing was carried out with a Walther Trowal TT25® centrifugal disk finishing unit. With WXC 6 x 6 mm triangular-shaped abrasive media, at 210 rpm, Ra = 6.3 μm is obtained in less than 5 min, Ra = 3.2 μm in 35 min. This batch also implies building tensile test samples and 10 x 10 x 20 mm^3 blocks to study material health. In the second production batch, two different samples were elaborated. The first corresponds to defect-free samples built with optimized parameters (Table 2). The notch tip radius equals two theoretical layer thicknesses; therefore, considering a processing zone larger than this radius, solicitated volume will include several layers and several melt pools. The second sample group corresponds to samples with deliberately deteriorated material. The second batch aimed to investigate the sensibility of the Charpy impact test to detect defects in a production batch. Defects intentionally introduced in samples consisted in a cubic lack of fusion of 300 μm side length. Due to technical limitations, these areas are scanned but using lower power settings (280 W) and higher scanning speed (2000 mm/s). This

Table 1 – Typical composition of Alloy 718 (UNS N07718) (w %).

C	Mn	Si	Co	Al	Ti	Nb	Mo	Cr	Fe	Ni
<0.08	<0.35	<0.35	<1	0.2–0.8	0.65–1.15	4.75–5.5	2.8–3.3	17–21	15–21	bal.

Table 2 – Manufacturing parameters for defect-free samples.

Laser power (W)	Laser scanning speed (mm/s)	Powder layer thickness (μm)	Hatch distance (μm)	Scanning rotation
370	1000	50	120 μm	67°

defect is probably too large to correspond to unoptimized process parameters [25,38]; however, it could correspond to a process interruption [39] or a high variation of received power during the process [18]. This high-power variation could result from a vapor plume or spatter droplets shadowing the powder bed during its laser irradiation or a damaged lens. Those defects also may correspond to a lack of fusion or a keyhole pore. The standard configuration consists of defects centered in the future fracture plane of the sample underneath the notch. Other configurations consist of defects shifted from this plane in 5 distinct groups. The samples-specific configuration will be detailed in section 2.2.

The chosen coordinate system is X and Y scanning directions of the laser, and Z is the build direction. All samples are built vertically on the platform (length of samples parallel to the Z direction, fracture surface in (X, Y) plane), using supports for easing extraction of samples and the ability to choose the height of the notch plane within the build job.

3. Methods

3.1. *Microstructural analysis*

Metallographic sample preparation was performed with a series of abrasive grinding papers with decreasing coarseness to 4000 grit, followed by diamond particle solutions of 3 and 1 μm and final polishing with an OP-S solution. Samples for microstructure observations were etched using 10% of oxalic acid under 3 V (DC) for 5 s and observed with an Optical Microscope (OM) Olympus PMG3. Fracture surface analysis was conducted using a Scanning Electron Microscope (SEM) ZEISS EVO10 HD15 equipped with a LaB_6 filament. The diaphragm was set to "depth" (aperture diameter of 20 μm) with an accelerating voltage of 15 kV, a probe current of 80 pA, and a Working Distance (WD) of 10 mm. Depth mode configuration on the ZEISS EVOHD15 SEM enables to have a better depth of focus which is convenient for performing fracture surface analysis.

3.2. *Mechanical analysis*

Tensile tests were performed using an INSTRON 5982 testing machine equipped with an AVE2 optical extensometer and a 100 kN load cell. Two painted dots, spaced by 10 mm, were taken as markers for optical strain measurement. Tensile samples were designed along the building direction with a dog bone shape, a 3x4 mm cross-section and a gauge length of 25 mm with a crosshead displacement of 1 mm/min. Due to the difficulty of measuring as-built samples' cross-section because of the high surface roughness, they were tested after a barrel finishing. Vickers hardness was measured using a ZWICK ZHU 2.5 durometer with a load of 10 kg and a distance of 750 μm between each hardness point. Tests were performed following EN ISO 6507–1 norm, and around 40 indents were performed on each condition. Charpy tests were carried out on 3 x 4 x 27 mm "miniature" specimens following the NF EN ISO 14556 (annexe D) standard (named KLST after the now cancelled DIN 50115 standard). Notches were obtained by milling, using a 60° chamfering/grooving carbide tool as a profile cutter. Microstructural changes were investigated by SEM-EBSD, and no significant change around the tip were noticed.

Two ideas govern the choice of such sample geometries. The first is that the test sample thickness has to be similar to LPBF-produced parts walls thickness. In this work, we considered 3–4 mm the acceptable limit. Candidates for such test specimens are ASTM E23 2.5 x 10 x 55 mm (thin cross-section), one-third sized ASTM E23 3.33 x 3.33 mm near-square section, and KLST 4 x 3 section. Indeed, a high aspect ratio cross-section implies predominant plane stress crack propagation and a relatively high shear fracture surface ratio. Near-square sections promote ductile tearing and in-plane strain and are believed to be more sensitive to material

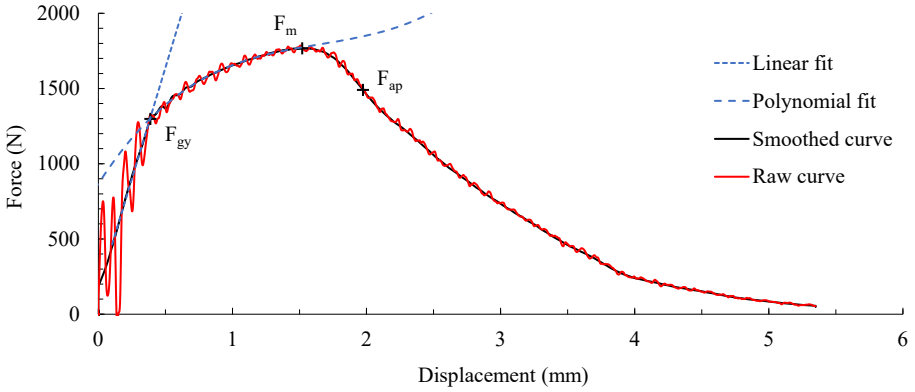

Fig. 1 – Force-displacement curve exploitation methodology. F_{gy} corresponds to the dynamic yield stress and F_m to the maximum force.

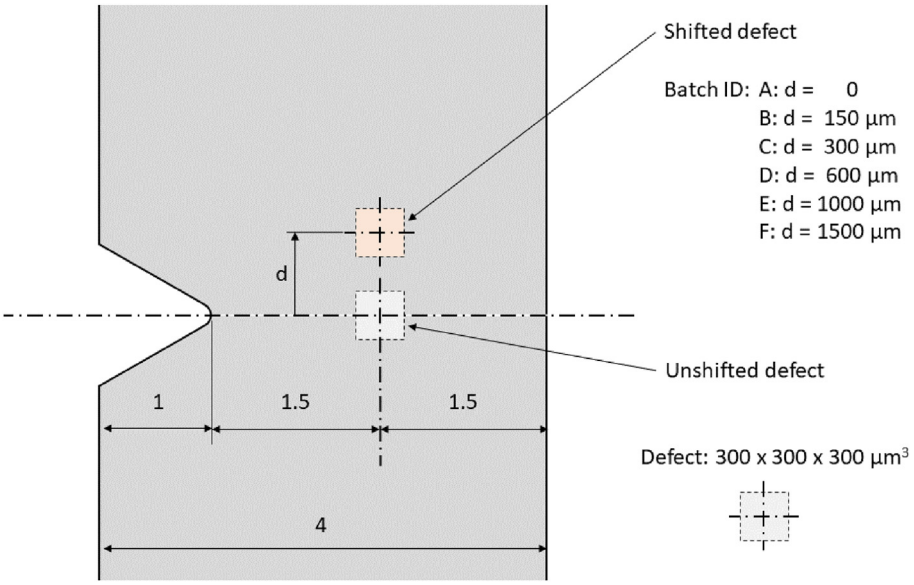

Fig. 2 – Representation of defects for batches A to F.

defects. The second point is that KLST samples are not strictly scaled down to 10 x 10 ASTM E23 samples and are easily manufactured. As broaching machines use 45° and not 60° V-broaches, the notch was machined using a carbide threat-cutting tool with a suitable 0.1 radius tip.

Furthermore, several models are proposed for a KLST to Charpy-V full-size samples data conversion. Such models allow the correction of upper shelf energy (ductile behavior) and ductile-to-brittle transition temperature for steels, as [40,41]. For ductile behavior, Lucon and coworkers conducted an extensive study on pressure vessel steels, proposing an exponential regression model between KLST and full-size 10 x 10 specimens' upper shelf energies [42].

Tests were carried out at room temperature with an instrumented Zwick/Roell HIT50P pendulum equipped with a C-type 50 J striker with a 2 mm radius. The span of anvils is adjusted to 22 mm for KLST samples. This instrumented apparatus was chosen to help understand behavior of the sample during impact. A load cell is an embedder in the striker, and an angular displacement sensor is mounted on the rotation axis, allowing the recording of force and displacement with a sampling frequency of 1 MHz.

Fig. 1 shows the different steps for analyzing force-displacement curves of Charpy impact tests. First, data were smoothed using a Savitzky-Golay filter with a polynomial of degree 5 and a width of 201 points per window. The force at the dynamic yield point F_{gy} was determined following NF EN ISO 14556 (annexe D.5) standard by the intersection of the Hooke's line (linear) fitted into the rising force data through the oscillations, and a third-degree polynomial fitted in the fully plastic range up to the maximal force value (F_m). The third-degree polynomial fit needs to be better defined in the abovementioned standard. Its start point was determined when a local linear regression performed on a sliding window of 20 smoothed data points gives a slope five times lower than the first.

An abrupt force drop in experimental data could identify an unstable propagation regime. This was not observed in the present study. Nevertheless, it was decided to determine the point of fastest force decrease in the crack propagation regime by the same regression on the 20 data points sliding window presented above. These point coordinates are (F_{ap}, S_{ap}).

The last aspect of post-F_{max} behavior is the smoothness of this propagation. Considering a fit of experimental smoothed data with a fifth-degree polynomial between F_m and the end of recorded data, R^2 and F-test (statistical test following Fisher law with a null hypothesis enabling the identification of the best fitting model) allow qualifying crack propagation within defective or sound material.

Statistical tests were performed to check the influence of parameters (surface finishing, defective batch, or not). An ANOVA test was performed, and a p-value was given as a result. ANOVA test works for a normal distribution of a population. Therefore, before performing the ANOVA test, the normality of distribution was checked with a Shapiro-Wilk test.

As stated above, the first defective configuration consists of a defect centered in the theoretical fracture plane. This configuration is noted A. However, defects are also shifted to check the sensitivity of their detection (Fig. 2). Serie B corresponds to a defect shifted out of the theoretical fracture plane by 150 µm. This configuration leads to an alignment of the defect "floor" in the fracture plane. Other series C, D, E, and F correspond respectively to 300, 600, 1000, and 1500 µm shifts, as shown in Fig. 2. Tomographic sections of generated defects are proposed in Fig. 3. The defect's actual position was precisely measured post-mortem either with a numerical microscope (Keyence VHX-7000) from the surface profile when the fracture surface intercepts the defect or by X-ray radiography (Easytom RX solutions, E=150 keV, pixel size of approx. 5 µm) when the defect is not evident on the fracture surface.

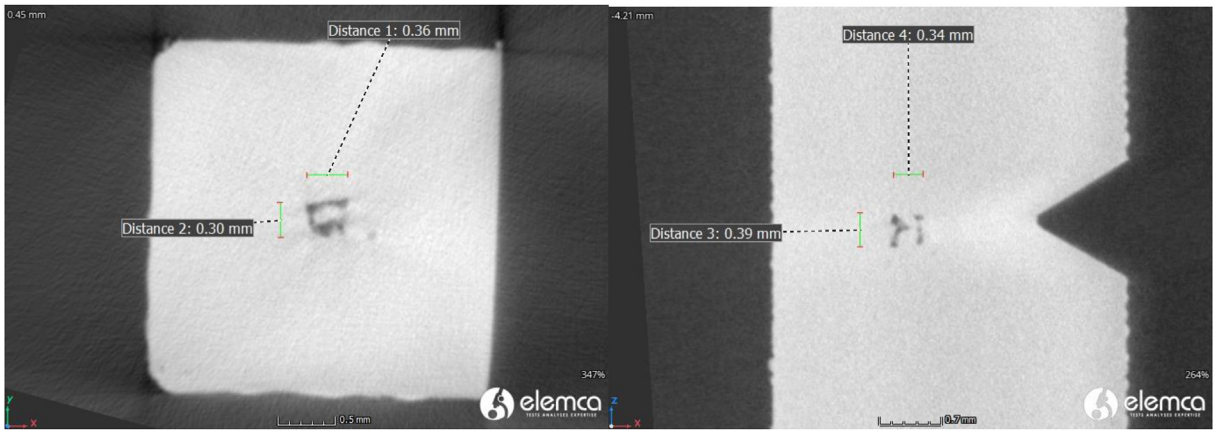

Fig. 3 – Tomographic sections of sample A25 evidencing created defect: section in building plane (a), section along building direction (b).

4. Results

4.1. *Materials characterization: porosity, microstructure, and mechanical properties of defect-free samples*

Microstructure corresponds to the one classically observed in the literature for IN718 produced by LPBF [13,29,43]. Laser-melted tracks appear through optical micrographs (Fig. 4). A typical columnar grain microstructure along the build direction can be observed. Fine dendrites (around 300 nm thickness measured from SEM images) can be distinguished from OM observations. Finally, some isolated pores exhibiting a diameter of 4–40 μm have been found [5,13]. Instabilities can explain those last on the melting pool engendered by a high scanning speed [5]. However, unlike observations from Xia et al. [5], pores do not seem to be concentrated at the laser-melted track or layer interfaces. This result confirms the high density of these samples and that they can consider defect-free production batches.

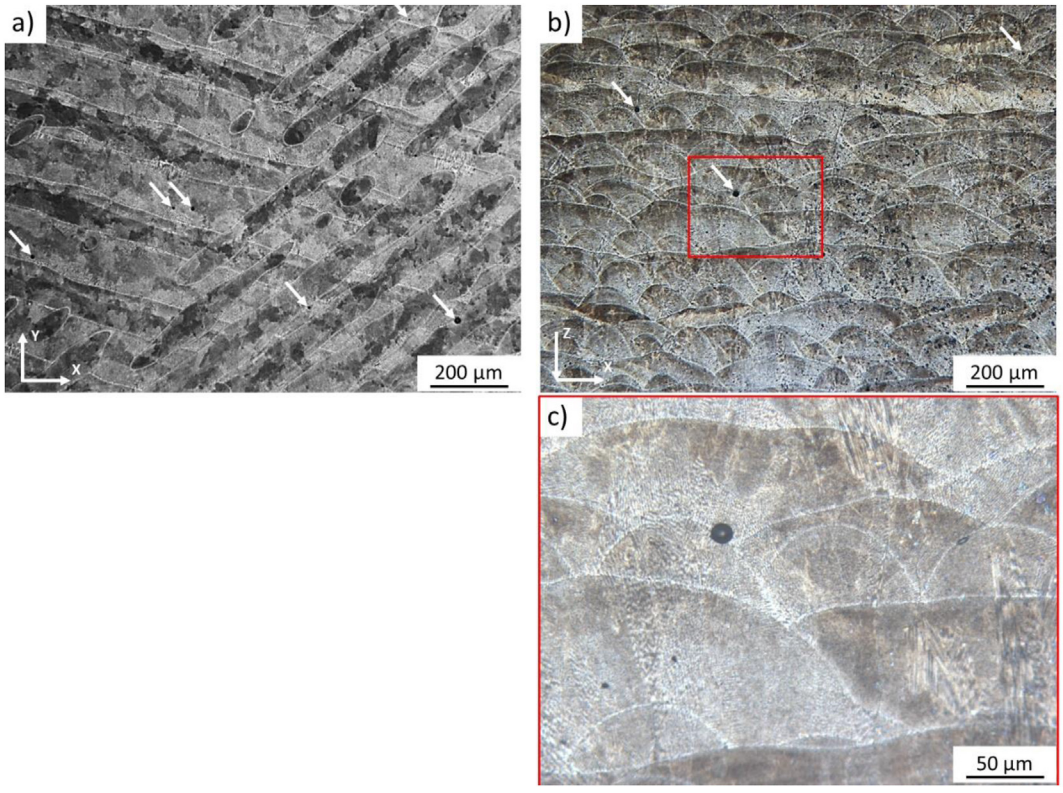

Fig. 4 – Optical micrographs of a) The scanned plan with laser tracks b) The build plan with melt pool depth; white arrows point pores c) enlarged view evidencing melt pools and grain structure.

First, to show that our material reaches the literature standard, tensile and hardness tests were performed. Considering tensile tests along the build direction exhibit a typical elastoplastic stress-strain curve (cf. Fig. 5), as already observed in the literature [9,23,29,30,33,44]. Samples were collected in different places on the building platform. We can observe excellent reproducibility irrespective of the surface roughness or the sample position on the building platform. Mechanical properties were extracted from the curves, and values are given in (Table 3). They are within the ranges reported in the literature. The only exception is total elongation at fracture, which is higher than in most studies. The slight curves dispersion proves the homogeneity of the build plate in terms of mechanical properties. This result is consistent with [45,46]. Therefore, in the following experiments, we will consider that sample position will not affect measured mechanical properties.

Vickers hardness measurements checked the anisotropy in the mechanical properties. Contrary to what is commonly observed in the literature [23,47], no anisotropy between both planes was measured (cf. Table 4). The indent diagonals are about 260 μm (more than a single melt pool, leading to a macro-scale analysis. This result can be explained by the scanning strategy leading to the potentially limited texture (cf. Fig. 4).

Even if the distribution of damage initiation sites also governs the ductile fracture, those dense samples with limited mechanical properties anisotropy seems suitable for designing the best conditions to perform the Charpy impact test.

4.2. *Influence of roughness on Charpy impact test*

For each roughness, eight Charpy impact samples were tested. Force-displacement curves were recorded and plotted in Fig. 6. All conditions show an elastoplastic behavior, and a quite good reproducibility is observed. Qualitatively, the surface finishing decreases the dispersion between curves. To compare the effect of surface finishing on force-displacement curves, the average curves from each Fig. 6 graph curve are calculated and plotted in Fig. 7. KLST samples appear to be sensitive to surface roughness. All curves are merged on the elastic part then a small dispersion on the plastic part is observed. Indeed, the maximal force (F_m) of KLST samples increases with the surface roughness. All curves are analyzed as explained above, and extracted results are displayed in Table 4. It is strongly suspected that the higher F_m of as-fabricated samples could be related to the notch machining process.

In addition to the curve analysis, fracture surfaces were observed. As observed by (Z. S [49]. on KLST samples, higher magnificent analysis reveals a typical ductile fracture with uniformly dispersed small dimples.

Typical fracture surfaces of KLST samples are displayed in Fig. 8. These samples exhibit a tearing surface with two

Table 3 – Tensile properties of alloy 718.

Reference	Direction	YS (MPa)	UTS (MPa)	ε_f (%)
Samples with R = 6.3 μm	Build	593 ± 3	928 ±2	35 ± 1
Samples with R = 3.2 μm	Build	608 ± 22	944 ± 7	37 ± 1
Litterature [9,23,29,30,33,44]	Build	572–711	845–1110	19–49

Table 4 – Vickers hardness values of as-built defect-free samples.

	This work	Literature [3,7,14,17,32,40,48]
Hardness XY	275 ± 8 HV_{10}	254-339 HV
Hardness XZ	275 ± 12 HV_{10}	281-320 HV

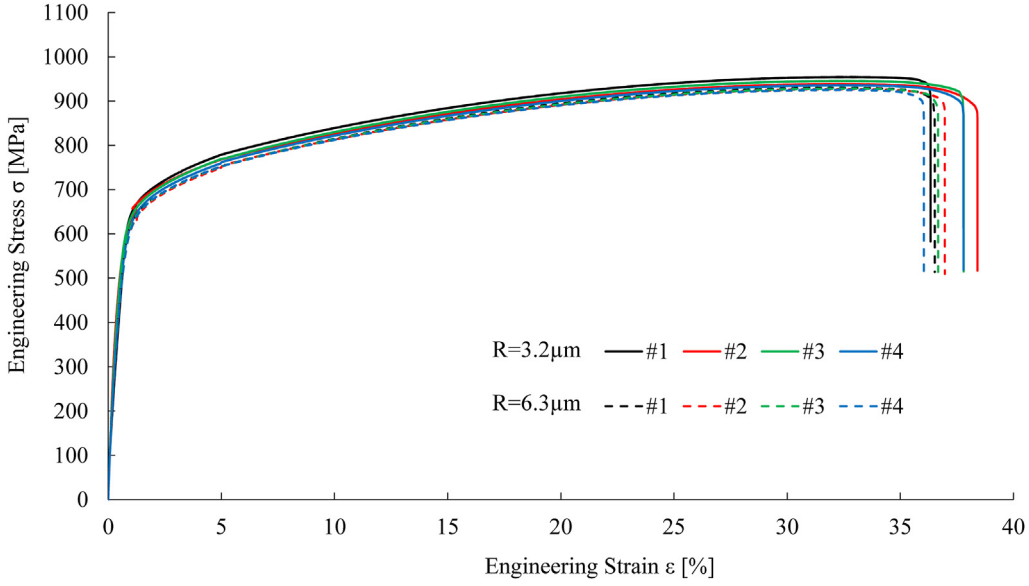

Fig. 5 – Engineering Stress–Strain curves of defect-free barrel finished samples.

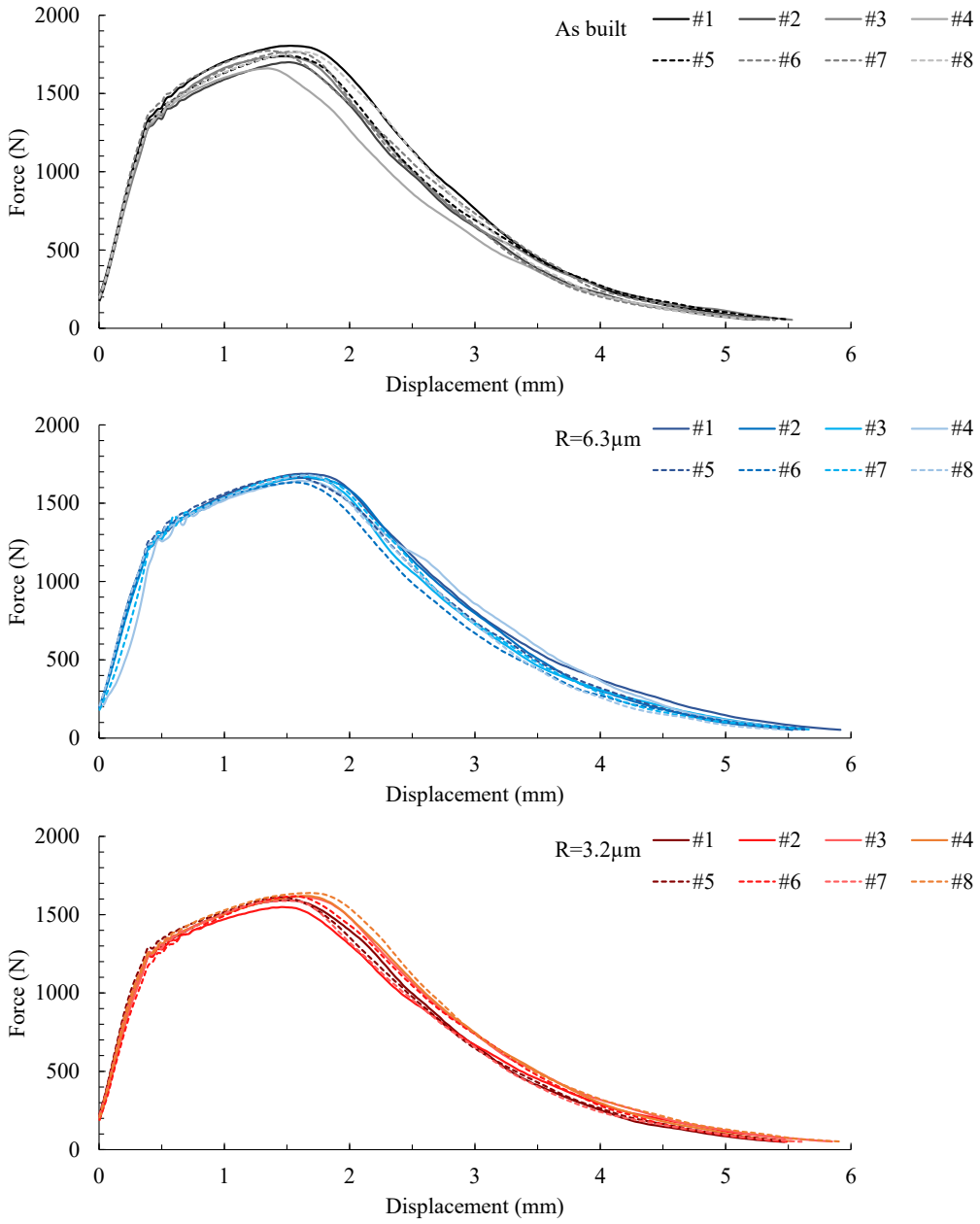

Fig. 6 – Force-Displacement curves for different surface finishing (as-built, Ra=6.3 μm, Ra=3.2 μm).

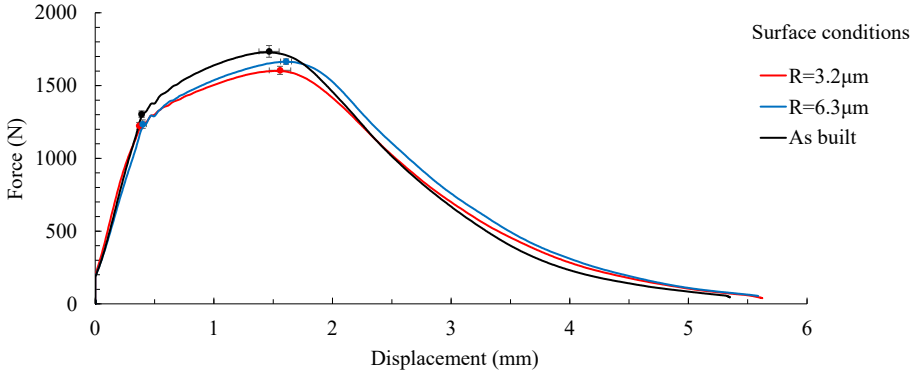

Fig. 7 – Average Force-Displacement curves for different surface finishing (as-built, Ra=6.3 μm, Ra=3.2 μm).

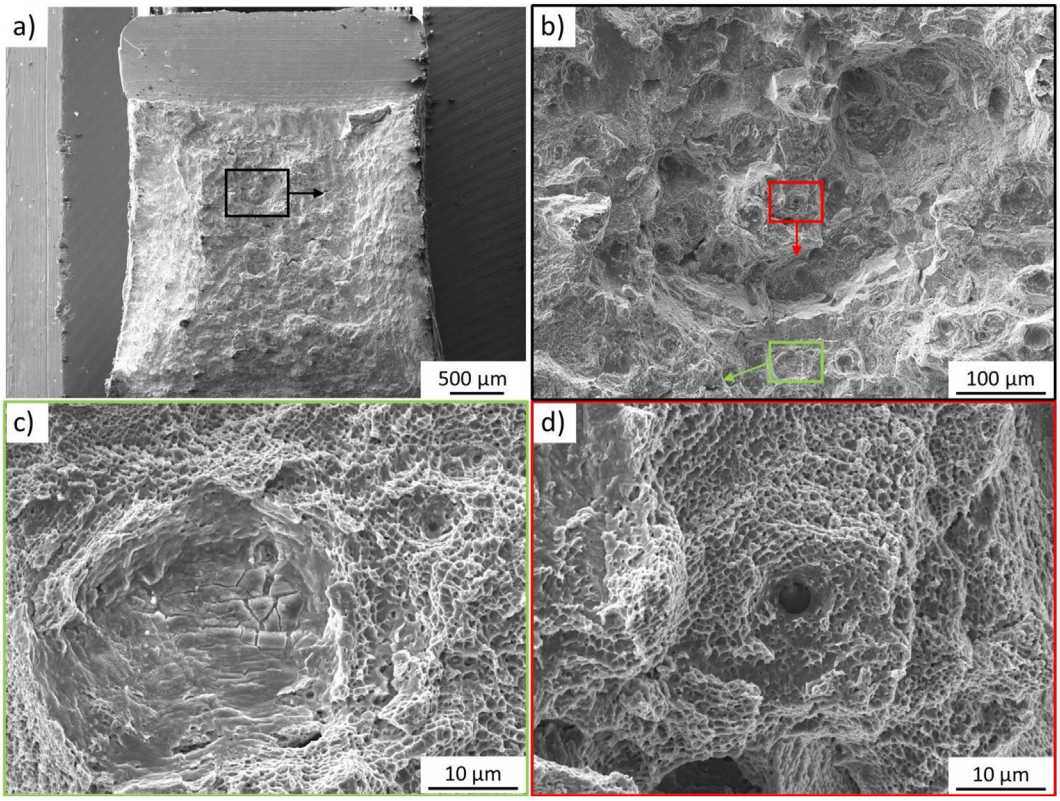

Fig. 8 – Fracture surface analysis of a KLST sample a) general appearance, b) center of the core area, and high magnification view of dimples c) around embedded brittle particle; and d) around the pore.

shearing lips. This is similar to low-magnification fracture surface analysis by Yu et al. (Z. S [49]. on as-build samples of 10 x 10 x 55 mm. KLST specimen, with a 3 x 3 mm fractured section, is mechanically similar to the typical Charpy sample of 10 x 8 mm and shows a real stress triaxiality, which leads to a more developed core area. Indeed, the tearing zone represents 65% of the entire section for the KLST samples. In the case of thick samples, the crack is mostly in plane-strain conditions. This leads to mode I plane-strain fracture condition (K_{Ic}), cited for most situations [50]. This could lead to more sensitivity to metallurgical defects for the KLST samples. Furthermore, higher magnification analysis reveals a similar dimpled surface than observed in the literature (Z. S [49]. Only a few dimples seemed coarser than usual and contained a brittle aluminum-rich particle, possibly a micron-scale alumina particle (Fig. 8c)). Other authors also observed these particles (H [51]. Finally, unlike Popovich et al. (V. A. [27], no sign of carbide particles has been found on fracture surfaces.

KLST samples enable reduced-size tests comparable to standard ASTM specimens, with natural stress triaxiality as standard Charpy impact test specimens. Moreover, this test is reproducible, and the impact of surface roughness is limited.

4.3. *Sensitivity of charpy impact test to detect a defective production batch*

4.3.1. *Defects centered in the fracture plane*

From the results presented above, we decided to investigate the sensitivity of the Charpy impact test to detect production batch defects with KLST geometry and surface roughness of 6.3 µm. Two observations govern the choice of this surface preparation. First, rough barrel finishing is not significantly time-consuming in the testing process; It allows a better sample positioning in a notch broaching machine, or in this case, the milling machine work-holder, ensuring notch depth closer to specifications. Second, the reduced roughness limits the wear phenomenon on Charpy testing machine anvils.

Force-displacement curves were recorded, and the average curves of fifteen tests were calculated and plotted in Fig. 9. Until the maximum force, mean curves are very close. However, the defect batch shows a higher slope in the propagation area. Therefore, it is possible to detect a defective batch from the curve.

Fracture surfaces of the defective sample were analyzed, revealing the cubic defect's shape and size. Fig. 10 c) allows us to examine the defect floor, presenting a smooth surface with a partially melted aggregate in its center, while Fig. 10 d) illustrates the reciprocal cavity.

4.3.2. *Influence of defect position on its detection*

Force-displacement curves were recorded for each batch, and the average curves of fifteen tests were calculated and plotted in Fig. 11. On elastic behavior, mean curves are all mixed up. First, divergences appear after the maximum force. Three different behaviors are observed: (i) A, B, and C batches, which show the same highest slope in the propagation area (ii) D batch with an intermediate slope, and (ii) E, F, and defect-free batched with the same behavior. Therefore, from the curves, it

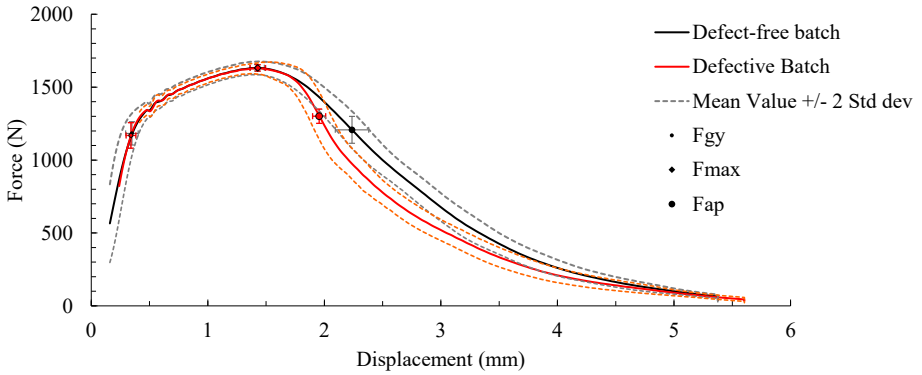

Fig. 9 – Average Force-Displacement curves for, respectively, defect-free samples batch and defective samples batch.

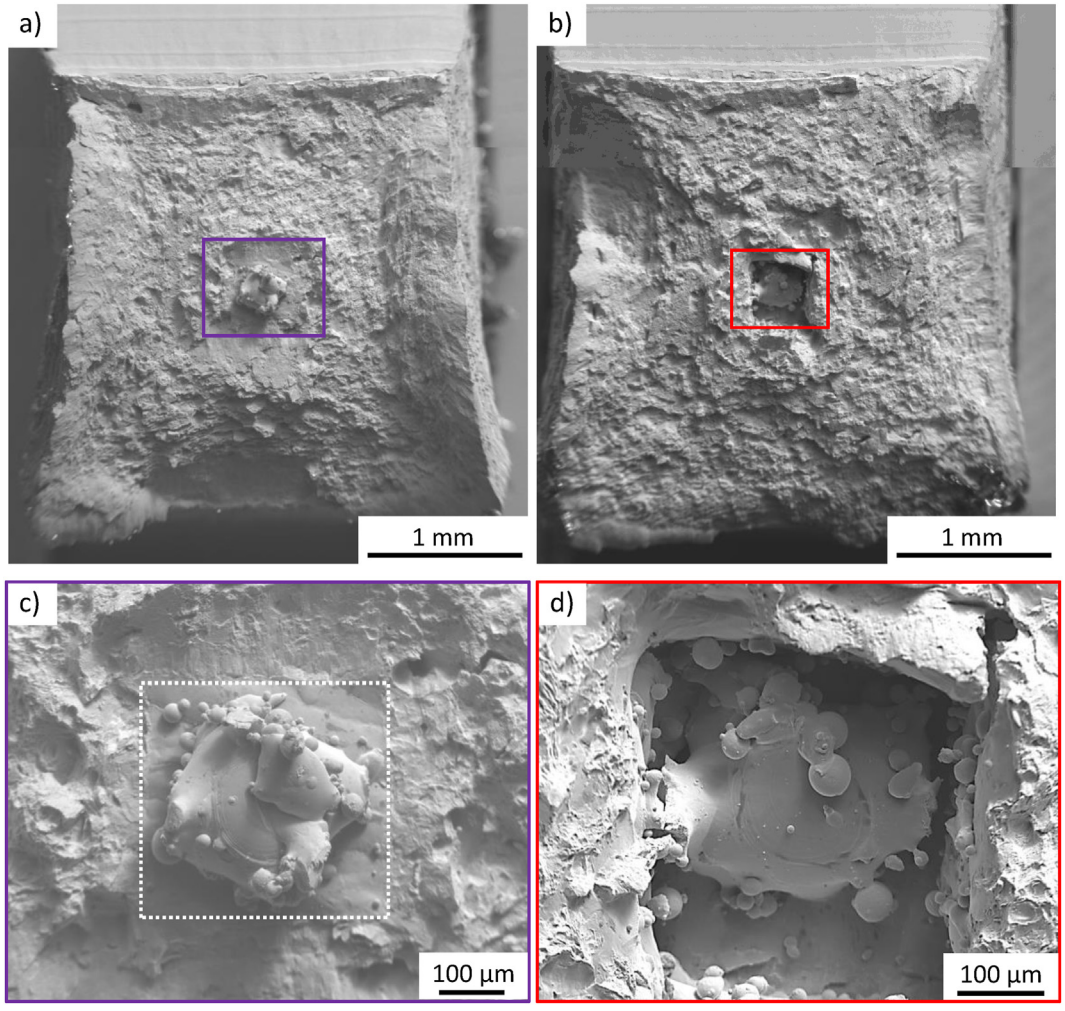

Fig. 10 – Secondary Electron imaging of defective samples' fracture surfaces: a) full view of sample A16 and b) D13; c) and d) high magnification of defect zone. The dotted square marks out the actual position of the defect area.

is possible to conclude that defects are detected in A, B, and C batches, and defects are not detected in E and F batches. It is more difficult to conclude about the D batch. One must notice that (F_{ap}, and S_{ap}) are logically influenced by defect presence, and the most visible difference is a significant diminution of S_{ap}. Statistical tests performed on each pair of batches confirms this statement. Indeed, F_{ap}, S_{ap}, and Resilience exhibit a substantial similarity for A, B, and C batches; as for Ref, E, and F batches, the D batch is only weakly similar to the Ref batch.

To overcome this uncertainty, the evolution of resilience for A, B, C, D, E, F, and defect-free batches with defect position is

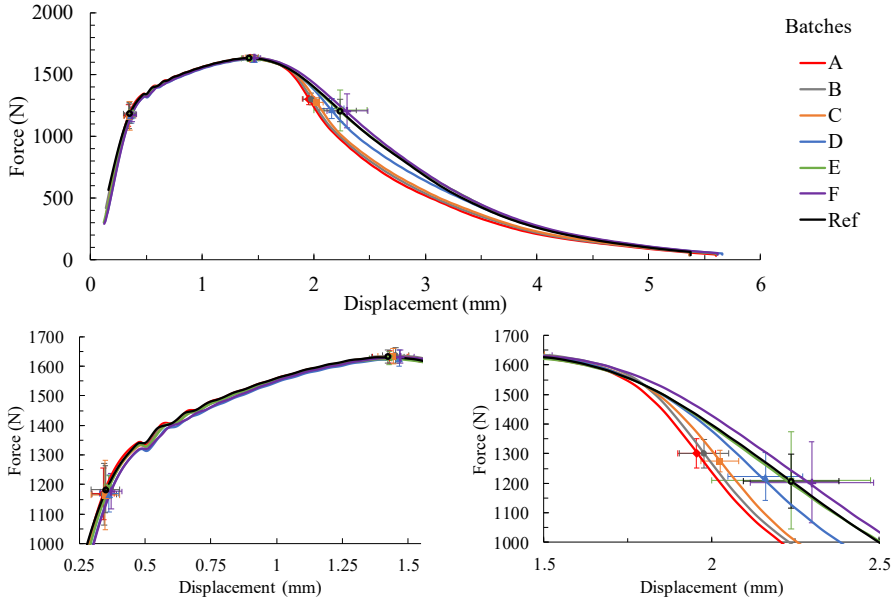

Fig. 11 – Average Force-Displacement curves for a defect-free samples batch (Ref) and A, B, C, D, E, F defective samples batches; Dynamic yield point, Maximum force, and Maximum force decrease rate points and their standard deviations are reported for each batch.

plotted in Fig. 12. Filled dots correspond to samples with defects visible on the fracture surface, hollowed dots to defects non-visible on the fracture surface, and bars to defect-free samples. Each color corresponds to a different sample batch.

First, resilience values for every batch show a significant dispersion (standard deviation is 2%–3% on resilience values for all batches except D) but are comparable to previous results. Second, dispersion of the defect position is also observed within a batch. It is to be noticed that the notch could not be strictly located at its nominal position due to a machining configuration involving the positioning of samples on their wavy top surface as a reference. Third, we can observe that the resilience increases when the defect positions shift exceeds 500 μm. Then resilience values for defect positions higher than 500 μm from the bottom of the notch show the same range as defect-free samples. However, due to the high-value dispersion, even for reference batch, this limit is difficult to be precisely determined.

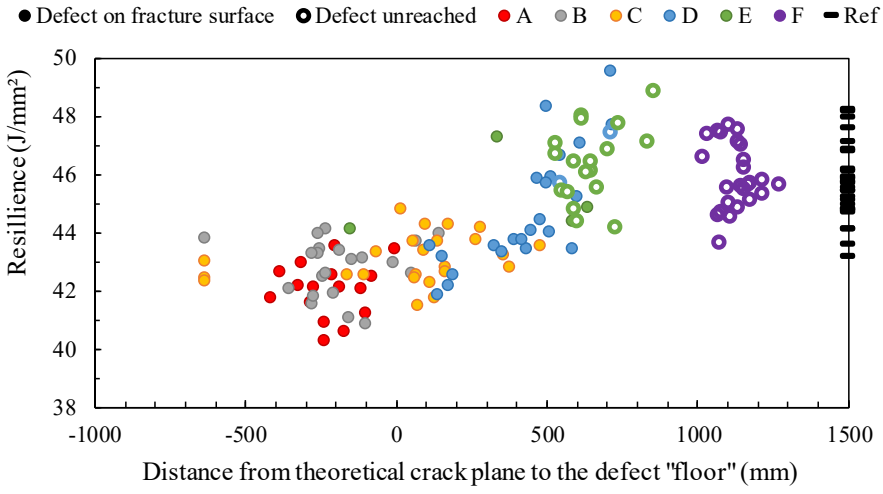

Fig. 12 – Evolution of resilience with defect position. Hollowed series correspond to the sample with a non-visible defect on the fracture surface, stated as an unreached defect. Their positions were determined by radiography. References data correspond to defect-free samples.

5. Discussion

5.1. *Influence of surface finishing on Charpy impact test results*

To evaluate the possibility to use samples with a reduced-size and with limited post-processing steps, the statistical difference between each series for each characteristic was evaluated with a p-value from an ANOVA test. ANOVA test enables us to distinguish if two series with close mean values and standard deviations are similar or different. Results are plotted in Table 5. The p-value of 0.05 is here set as the limit between statistically different batches' behavior.

Energy and resilience values are not statistically different depending on surface roughness. However, for values extracted from the curve, no one can be considered statistically similar. It highlights the dispersion observed in Fig. 7. The statistical difference noticed for the dynamic yield force F_{gy} is imputed to a dispersion of samples/notch geometry measurement issues influenced by surface finishing. The high roughness of as fabricated samples could imply that adequate notch depth is lesser than expected because of the disturbed reference surface employed during machining and measuring. Hence, the actual cross-section of samples is slightly higher than intended and could explain the behavior of these samples, slightly above the two-barrel surface finish. It is consistent with the neglectable influence of surface roughness on additive manufactured materials' tensile properties [52,53].

These results assess the possibility of using reduced-size geometry (KLST samples) to evaluate a quality batch. However, samples/notch geometry depends on surface finishing post-treatment, and the plastic part with the maximum force shows a dispersion; therefore, batch quality evaluation must be performed by using the same surface finishing treatment.

5.2. *Sensibility of Charpy impact test to detect a defective production batch*

Let us now discuss the sensibility of the Charpy impact test to detect a defective production batch. The resulting defect is a cubic area with a 300 μm side. The defect is located between the notch and the opposite side, corresponding to 10% of the ligament. Its projected area is 1% of the sample cross-section. As observed in Table 6, only a resilience value is necessary to detect a large defect localized within the crack plane, materialized by the notch tip. A decrease of around 10% of resilience is observed. Therefore, a non-instrumented Charpy test may be sufficient to detect this kind of defect. Moreover, this test is efficiently checking the batch quality when a local defect is suspected. The reduced size of sample tests enables a little loose of matter to check the reliability of the batch. If we want to evaluate the efficiency of the Charpy test on KLST, 6.3 μm barrel finished samples, the energy, the resilience, F_{gy}, and F_m stress are given in Table 5. From this table, if we look to the average and standard deviation, all series seem similar. Therefore, average and standard deviation are not enough powerful to conclude. Consequently, to understand if a defective batch is statistically similar to the non-defect reference batch, we consider similar series (defect not detected) if p-value given by the ANOVA test is >0.05 and figures are plotted in red, very different series (defect detected) for p-value <0.01 (plotted in green) and different series (defect suspected) for 0.01<p<0.05 (plotted in blue)First, the statistical similarity of dynamic yield strength highlights that defect has a discernible influence only on the crack propagation regime after reaching F_m (all F_{gy} and F_m are considered similar series). This assumption is in accordance with Fadida et al. investigations of defect presence by high strain rate compressive test [20]. Second that it was not possible to detect a defect in batches E and F. In the opposite, the statistical similarity of batches A, B and C with reference is consistent with the similar defect position observed in previous figures. Third, the energy, resilience, and F_{ap} are statistically different from references for A, B, C, and D series. This last point confirms the difference observed on curves from Fig. 9 and proves a Charpy test's efficiency in detecting a defective batch. Moreover, the difference between reference and defect batch values is decreasing with the defect shift (see Table 7).

However, analysis of resilience as a function of defect shift needs to provide a clear threshold in a reached or unreached defect. Indeed, it is proposed that defect shift generates a weak inflection of crack propagation by disturbing strain fields around the crack tip. Deviation of the crack path possibly generates a slight increase in fracture surface area, inducing an increasing resilience value as the defect is shifted farther and farther. Once the defect is too far from the crack path, its effect becomes negligible and measured resilience levels are comparable to the reference batch. This deflection of the crack path is evidenced thanks to numerical microscope measurements of fracture surfaces (Fig. 13). Here, for a batch D sample, the crack path is significantly modified by defect compared to a batch A one.

To obtain a fair value of the maximum shift allowing detection of the defect, F-test performed on the 5th-degree

Table 5 – Charpy impact test values extracted from individual tests smoothed curves (see Fig. 6) for three surface conditions.

		KLST samples surface condition		
		As-built	Ra = 6.3 μm	Ra = 3.2 μm
Energy	(J)	4.49±0.17	4.62±0.12	4.44 ± 0.14
Resilience	(J/cm^2)	45.8±1.7	47.9±1.3	47.0 ± 1.4
F_{gy}	(N)	1303±23	1235±29	1224 ± 23
S_{gy}	(mm)	0.39±0.02	0.40±0.03	0.37 ± 0.01
F_m	(N)	1735±39	1666±17	1605 ± 26

Table 6 – P-value for each characteristic value for different surface finishing.

	KLST samples, all surface conditions	
	p-value	Statistically different?
Energy (J)	0.105	no
Resilience (J/cm^2)	0.070	no
F_{gy} (N)	<0.001	yes
F_m (N)	<0.001	yes

Table 7 – Charpy impact test values extracted from individual tests smoothed curves (see Fig. 6) for comparing defective and defect-free (reference) batches. P-values were calculated with reference batch, and the red color corresponds to p>0.05 (similar series), green color to p<0.01(very different series), and blue to 0.01<p<0.05 (slightly different series).

	Reference	Batch (A)	Batch (B)	Batch (C)	Batch (D)	Batch (E)	Batch (F)
Energy (J)	4.4 ± 0.2	4.3 ± 0.2	4.0±0.3	4.2±0.1	4.3±0.2	4.3±0.2	4.5±0.2
Resilience (J/cm²)	46± 2	42 ± 2	42±3	43±1	44±2	46±2	46±2
F_{gy} (N)	**1184±80**	**1170±87**	1152±113	1164±118	1155±83	1192±38	1176±60
F_m (N)	**1633±22**	**1632±22**	1637±25	1635±26	1628±28	1628±23	1633±22
F_{ap} (N)	**1208±92**	**1301±49**	1300±48	1275±36	1222±82	1210±165	1203±137

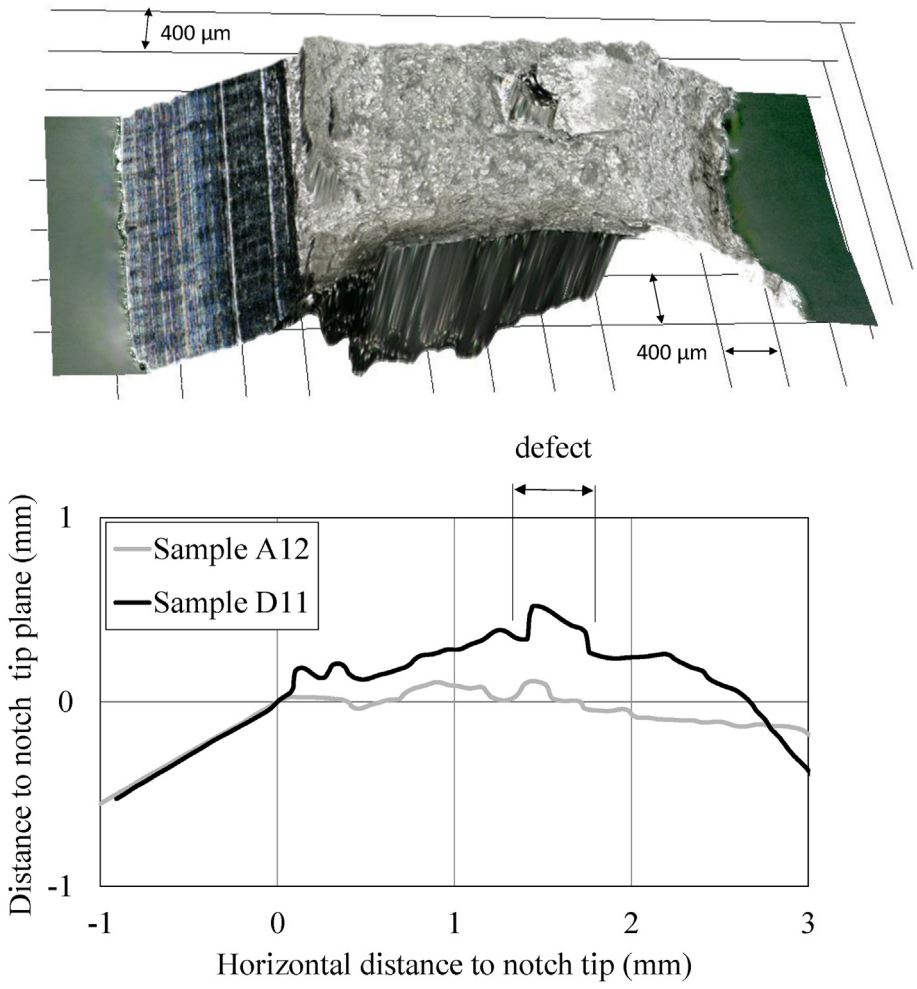

Fig. 13 – Fracture surface view of sample A12 and profiles measurements in the median plane of A12 and D11 samples.

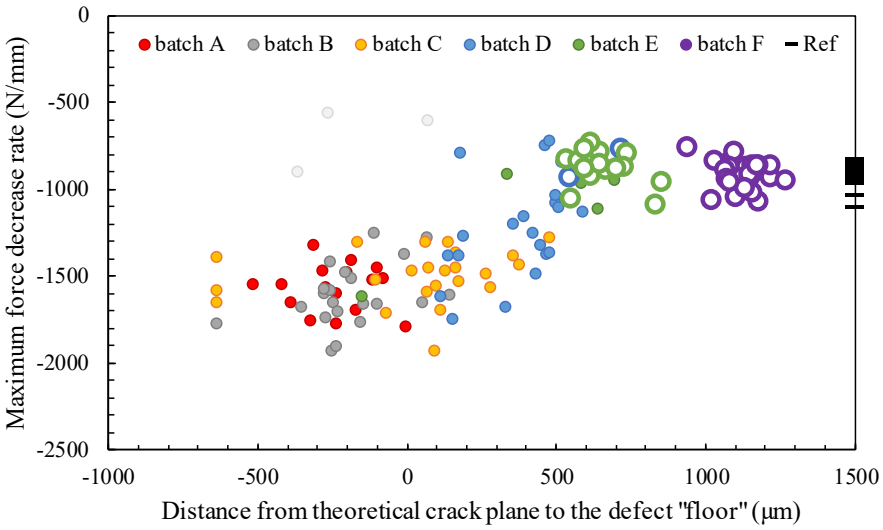

Fig. 14 – Effect of defect position on maximum force decrease rate in propagation regime. Shaded dots represent odd data, as incoherent force-displacement curves and/or excessive resilience recorded values. These are not taken into account in subsequent analysis.

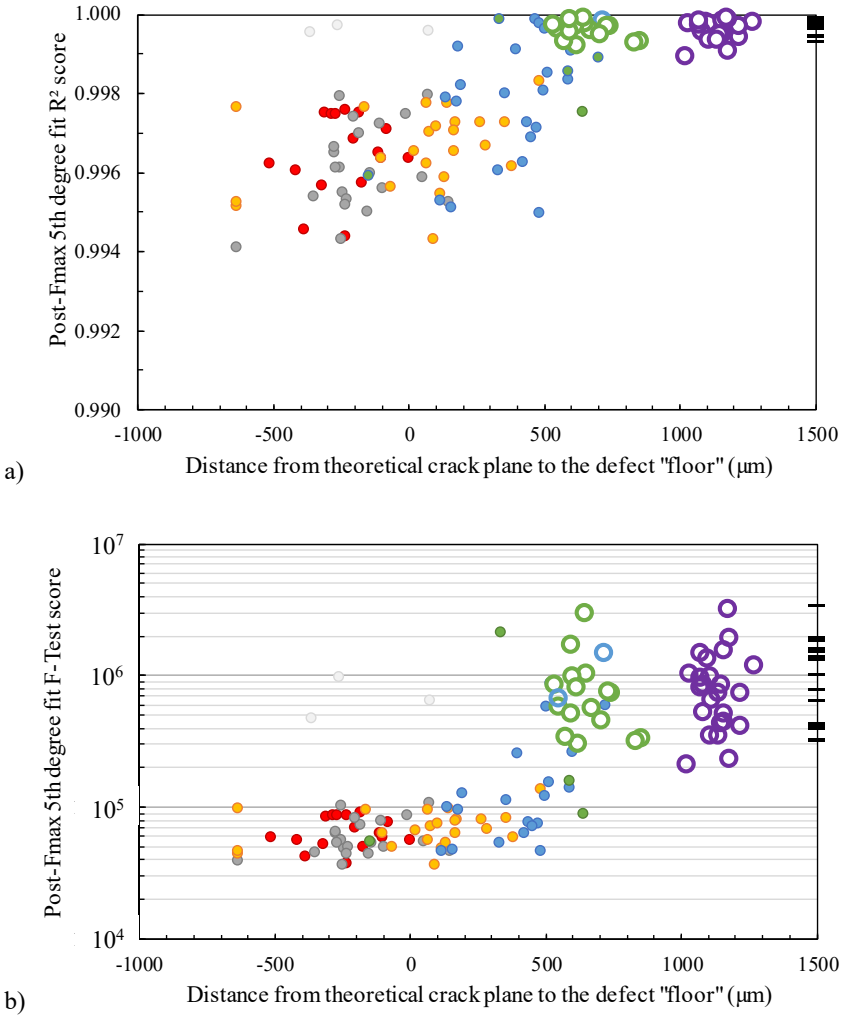

Fig. 15 – Results of 5th-degree polynomial fit performed on force-displacement data after maximum force: (a) R^2 score; (b) F-test score.

polynomial fit appears to be conclusive. From the analysis of Fig. 15-b, it is possible to assume that the maximum offset of the detected defect is approx. 500 μm. However, it is necessary to check those other behavior indicators as F_m and F_{gy} are comparable to sound samples' mean values. Indeed, some tests proved to satisfy this post-F_m smooth behavior with a defect on their fracture surface. However, they consistently failed to reach the abovementioned criterion, exhibiting a significantly low resilience value.

To go further on the behavior of defective samples, the evaluation of the maximum force decrease rate versus the actual position of defects is presented in Fig. 14. It helps in understanding how defect affects the crack propagation regime. So, batches A to C exhibited a significantly higher force decrease rate (-1565 N mm^{-1} ± 164) than E, F, and Reference batches (-924 N mm^{-1} ± 124). The force decrease rate seems to be strongly correlated to the presence of the defect on the fracture surface or not. Indeed, only few samples have a relatively low force decrease rate and a defect visible on the fracture surface.

It is also proposed to evaluate the progressiveness of crack propagation via the modeling of force-displacement curves. In this way, the results of the 5th-degree polynomial fit performed on post-F_m data are proposed in Fig. 15. Examining Fig. 15-a allows us to assume that if a defect is not visible on the fracture surface, so considered unreached, R^2 is approx. 0.999 or better. However, F-test gives a better understanding of model accuracy (Fig. 15-b). F-test scores are 2.10^5 and 3.10^6 for unreached or no defects, and very few reached defects generate F-test better than this level. Batches A, B, and C do not present an F-test scores better than 10^5.

6. Conclusion

This paper investigates using the Charpy impact test as a certification test for a production batch. First, the best conditions for surface finishing and then the Charpy impact test results from one reference batch (defect-free) and one defective batch were compared. Hereinbelow are the main conclusions.

These KLST samples give reproducible values and curves clean enough to be analyzed. Searching for the most cost-effective sample preparation for the most reproducible testing, different surface conditions were explored. It was found that surface roughness has a limited impact on the resilience tests on extracted values, but the standard deviations are lower for lightly barrel-finished samples.

Investigated defects are cube-shaped lack of fusion produced in a controlled manner, which tried to represent discrete defects like keyhole pore or lack of fusion.

This detection does not need an instrumented pendulum. Considering the defect detection, resilience is decreased by approx. 10% for defective batches in which the defect can be detected, compared to a defect-free batch. Another way to easily detect a defect thanks to Charpy test is to observe the surface fracture: a defect may be visible if crack is deviated. Furthermore, defects are detected in the present configuration until 500 μm off the notch tip.

Using an instrumented pendulum, additional data may be extracted. Defect presence affects measured material behavior only in the propagation regime after F_m. Considering that the Force decrease rate can describe some aspects of crack propagation, the maximum force decrease rate indicates an accelerated propagation for defective batches in the early stages of cracking. Investigation of crack propagation's smoothness helped to determine the range of detectable defects. Furthermore, defects are detected in the present configuration until 500 μm off the notch tip.

In the context of "real" production batches, defects type can be identified thanks to fracture surface analysis of resilience samples and will help determine their real harmfulness.

Declaration of competing interest

The authors declare the following financial interests/personal relationships which may be considered as potential competing interests: Joel ALEXIS reports financial support was provided by Région Occitanie. Arnaud VOTIE reports financial support was provided by Région Occitanie. Jean-Marc CLOUE reports financial support was provided by Région Occitanie.

Acknowledgments

The authors would like to acknowledge the Région Occitanie as funding support, Liebherr Aerospace Toulouse, Freyssinet AéroEquipment, and Spinodal Conseil partners of the FASTER project in which these investigations took place. Thanks to Frédéric Letrange from Liebherr Aerospace for supporting the project and helping with initial defect detection by tomography. The authors would like to thank also students who contributed to this work: Vanina Pelouard for designing production batches and exploring barrel finishing, Lukas Heinze for helping study the effects of surface conditions, Axel Bruel, Rémi Lapuyade, and Jérémie Saint-Lo for performing the test on different defectives batches.

REFERENCES

[1] Caiazzo Fabrizia, Alfieri Vittorio, Corrado Gaetano, Argenio Paolo. Laser powder-bed fusion of inconel 718 to manufacture turbine blades. Int J Adv Des Manuf Technol 2017;93(9):4023–31. https://doi.org/10.1007/s00170-017-0839-3.

[2] Zhang Dongyun, Wen Niu, Cao Xuanyang, Liu Zhen. Effect of standard heat treatment on the microstructure and mechanical properties of selective laser melting manufactured inconel 718 superalloy. Mater Sci Eng, A 2015;644(September):32–40. https://doi.org/10.1016/j.msea.2015.06.021.

[3] Ardila LC, Garciandia F, González-Díaz JB, Álvarez P, Echeverria A, Petite MM, et al. "Effect of IN718 recycled powder reuse on properties of parts manufactured by means of selective laser melting.". Physics procedia, 8th international conference on laser assisted net shape engineering LANE 2014 2014;56:99–107. https://doi.org/10.1016/j.phpro.2014.08.152. January.

[4] Aydinöz ME, Brenne F, Schaper M, Schaak C, Tillmann W, Nellesen J, et al. On the microstructural and mechanical properties of post-treated additively manufactured inconel 718 superalloy under quasi-static and cyclic loading. Mater Sci Eng, A 2016;669(July):246–58. https://doi.org/10.1016/j.msea.2016.05.089.
[5] Xia Mujian, Gu Dongdong, Yu Guanqun, Dai Donghua, Chen Hongyu, Shi Qimin. Porosity evolution and its thermodynamic mechanism of randomly packed powder-bed during selective laser melting of inconel 718 alloy. Int J Mach Tool Manufact 2017;116(May):96–106. https://doi.org/10.1016/j.ijmachtools.2017.01.005.
[6] Chen Yuan, Lu Fenggui, Zhang Ke, Nie Pulin, , Seyed Reza Elmi Hosseini, Feng Kai, Li Zhuguo. Dendritic microstructure and hot cracking of laser additive manufactured inconel 718 under improved base cooling. J Alloys Compd 2016;670(June):312–21. https://doi.org/10.1016/j.jallcom.2016.01.250.
[7] Jia Qingbo, Gu Dongdong. Selective laser melting additive manufacturing of inconel 718 superalloy parts: densification, microstructure and properties. J Alloys Compd 2014;585(February):713–21. https://doi.org/10.1016/j.jallcom.2013.09.171.
[8] Li Shuai, Wei Qingsong, Zhang D, Chua Kai. In: "Microstructures and texture of inconel 718 alloy fabricated by selective laser melting."; 2014. p. 139–44. https://doi.org/10.3850/978-981-09-0446-3_021.
[9] Vilaro T, Colin C, Bartout JD, Nazé L, Sennour M. Microstructural and mechanical approaches of the selective laser melting process applied to a nickel-base superalloy. Mater Sci Eng, A 2012;534(February):446–51. https://doi.org/10.1016/j.msea.2011.11.092.
[10] M'Saoubi Rachid, Larsson Tommy, Outeiro José, Guo Yang, Sergey Suslov, Saldana Christopher, et al. Surface integrity analysis of machined inconel 718 over multiple length scales. CIRP Annals 2012;61(1):99–102. https://doi.org/10.1016/j.cirp.2012.03.058.
[11] Ulutan Durul, Özel Tuğrul. Machining induced surface integrity in titanium and nickel alloys: a review. Int J Mach Tool Manufact 2011;51(March):250–80. https://doi.org/10.1016/j.ijmachtools.2010.11.003.
[12] Yazid MZA, CheHaron CH, Ghani JA, Ibrahim GA, Said AYM. Surface integrity of inconel 718 when finish turning with PVD coated carbide tool under MQL. Procedia Engineering, 1st CIRP Conference on Surface Integrity (CSI) 2011;19(January):396–401.
[13] Choi Joon-Phil, Shin Gi-Hun, Yang Sangsun, Yang Dong-Yeol, Lee Jai-Sung, Brochu Mathieu, et al. Densification and microstructural investigation of inconel 718 parts fabricated by selective laser melting. Powder Technol 2017;310(April):60–6. https://doi.org/10.1016/j.powtec.2017.01.030.
[14] Yang Xuan, Li Yazhi, Li Biao. Formation mechanisms of lack of fusion and keyhole-induced pore defects in laser powder bed fusion process: a numerical study. Int J Therm Sci 2023;188(June):108221.
[15] Grasso Marco, Colosimo Bianca Maria. Process defects and in situ monitoring methods in metal powder bed fusion: a review. Meas Sci Technol 2017;28(4):044005. https://doi.org/10.1088/1361-6501/aa5c4f.
[16] Simpson Timothy W. Postprocessing steps and costs for metal 3D printing. Addit Manuf 2018. May 21, 2018, https://www.additivemanufacturing.media/articles/postprocessing-steps-and-costs-for-metal-3d-printing.
[17] Raoufi Kamyar, Haapala Karl R, Etheridge Tom, Manoharan Sriram, Paul Brian K. Cost and environmental impact assessment of stainless steel microscale chemical reactor components using conventional and additive manufacturing processes. J Manuf Syst 2022;62(January):202–17. https://doi.org/10.1016/j.jmsy.2021.11.017.
[18] Gong Haijun, Rafi Khalid, Gu Hengfeng, Janaki Ram GD, Starr Thomas, Brent Stucker. Influence of defects on mechanical properties of Ti–6Al–4V components produced by selective laser melting and Electron beam melting. Mater Des 2015;86(December):545–54. https://doi.org/10.1016/j.matdes.2015.07.147.
[19] Wits Wessel W, Carmignato Simone, Zanini Filippo, Vaneker Tom HJ. Porosity testing methods for the quality assessment of selective laser melted parts. CIRP Annals 2016;65(1):201–4. https://doi.org/10.1016/j.cirp.2016.04.054.
[20] Fadida Refael, Rittel Daniel, Shirizly Amnon. Dynamic mechanical behavior of additively manufactured Ti6Al4V with controlled voids. J Appl Mech 2015;82(4):041004. https://doi.org/10.1115/1.4029745.
[21] Yang Teng, Mazumder Sangram, Jin Yuqi, Brian Squires, Sofield Mathew, Pantawane Mangesh V, et al. A review of diagnostics methodologies for metal additive manufacturing processes and products. Materials 2021;14(17):4929.
[22] Schirra John Joseph, Huse Caless Robert, Hatala Robert W. The effect of Laves phase on the mechanical properties of wrought and cast + HIP inconel 718. https://doi.org/10.7449/1991/Superalloys_1991_375_388; 1991.
[23] Chlebus E, Gruber K, Kuźnicka B, Kurzac J, Kurzynowski T. Effect of heat treatment on the microstructure and mechanical properties of inconel 718 processed by selective laser melting. Mater Sci Eng, A 2015;639(July):647–55. https://doi.org/10.1016/j.msea.2015.05.035.
[24] Komarasamy Mageshwari, Shukla Shivakant, Williams Sarah, Kumar Kandasamy, Kelly Shawn, Rajiv S, et al. Microstructure, fatigue, and impact toughness properties of additively manufactured nickel alloy 718. Addit Manuf 2019;28(August):661–75. https://doi.org/10.1016/j.addma.2019.06.009.
[25] Lu Yanjin, Wu Songquan, Gan Yiliang, Huang Tingting, Yang Chuanguang, Lin Junjie, et al. Study on the microstructure, mechanical property and residual stress of SLM inconel-718 alloy manufactured by differing island scanning strategy. Opt Laser Technol 2015;75(December):197–206. https://doi.org/10.1016/j.optlastec.2015.07.009.
[26] Neikter M, Raja DC, Balachandramurthi AR, Harlin P. Tailored ductility and strength for enhanced impact toughness of laser powder fusion built alloy 718. J Alloys Compd 2021;884(December):161374. https://doi.org/10.1016/j.jallcom.2021.161374.
[27] Popovich VA, Borisov EV, Popovich AA, Sufiiarov V Sh, Masaylo DV, Alzina L. Impact of heat treatment on mechanical behaviour of inconel 718 processed with tailored microstructure by selective laser melting. Mater Des 2017;131(October):12–22. https://doi.org/10.1016/j.matdes.2017.05.065.
[28] Tucho Wakshum M, Cuvillier Priscille, Sjolyst-Kverneland Atle, Hansen Vidar. Microstructure and hardness studies of inconel 718 manufactured by selective laser melting before and after solution heat treatment. Mater Sci Eng, A 2017;689(March):220–32. https://doi.org/10.1016/j.msea.2017.02.062.
[29] Ni Mang, Chen Chao, Wang Xiaojun, Wang Pengwei, Li Ruidi, Zhang Xiaoyong, et al. Anisotropic tensile behavior of in situ precipitation strengthened inconel 718 fabricated by additive manufacturing. Mater Sci Eng, A 2017;701(July):344–51. https://doi.org/10.1016/j.msea.2017.06.098.

[30] Paccou Elie, Mokhtari Morgane, Keller Clément, Nguejio Josiane, Williams Lefebvre, Sauvage Xavier, et al. Investigations of powder reusing on microstructure and mechanical properties of inconel 718 obtained by additive manufacturing. Mater Sci Eng, A 2021;828(November):142113. https://doi.org/10.1016/j.msea.2021.142113.

[31] Popovich Anatoly A, Sh Sufiiarov Vadim, Polozov Igor A, Borisov Evgenii V. Microstructure and mechanical properties of inconel 718 produced by SLM and subsequent heat treatment. Key Eng Mater 2015;651–653:665. https://doi.org/10.4028/www.scientific.net/KEM.651-653.665. 70.

[32] Sufiiarov V Sh, Popovich AA, Borisov EV, Polozov IA, Masaylo DV, Orlov AV. The effect of layer thickness at selective laser melting. Procedia Engineering, 13th Global Congress on Manufacturing and Management Zhengzhou 2017;174(January):126–34. https://doi.org/10.1016/j.proeng.2017.01.179. China 28-30 November, 2016.

[33] Vieille B, Keller C, Mokhtari M, Briatta H, Breteau T, Nguejio J, et al. Investigations on the fracture behavior of inconel 718 superalloys obtained from cast and additive manufacturing processes. Mater Sci Eng, A 2020;790(July):139666. https://doi.org/10.1016/j.msea.2020.139666.

[34] Park So-Yeon, Kim Kyu-Sik, Kim Min-Cheol, Kassner Michael E, Lee Kee-Ahn. Effect of post-heat treatment on the tensile and cryogenic impact toughness properties of inconel 718 manufactured by selective laser melting. Adv Eng Mater 2021;23(3):2001005. https://doi.org/10.1002/adem.202001005.

[35] Lesyk DA, Martinez S, Mordyuk BN, Dzhemelinskyi VV, Lamikiz A, Prokopenko GI. Post-processing of the inconel 718 alloy parts fabricated by selective laser melting: effects of mechanical surface treatments on surface topography, porosity, hardness and residual stress. Surf Coating Technol 2020;381(January):125136. https://doi.org/10.1016/j.surfcoat.2019.125136.

[36] Liu Fencheng, Lin Xin, Yang Gaolin, Song Menghua, Chen Jing, Huang Weidong. Microstructure and residual stress of laser rapid formed inconel 718 nickel-base superalloy. Opt Laser Technol 2011;43(1):208–13. https://doi.org/10.1016/j.optlastec.2010.06.015.

[37] Rangaswamy P, Griffith ML, Prime MB, Holden TM, Rogge RB, Edwards JM, et al. Residual stresses in LENS® components using neutron diffraction and contour method. Mater Sci Eng: A, Measurement and Interpretation of Internal/Residual Stresses 2005;399(1):72–83. https://doi.org/10.1016/j.msea.2005.02.019.

[38] Hilaire Alexandra, Andrieu Eric, Wu Xinhua. High-temperature mechanical properties of alloy 718 produced by laser powder bed fusion with different processing parameters. Addit Manuf 2019;26(March):147–60. https://doi.org/10.1016/j.addma.2019.01.012.

[39] Stoll Philipp, Spierings Adriaan, Wegener Konrad. Impact of a process interruption on tensile properties of SS 316L parts and hybrid parts produced with selective laser melting. Int J Adv Des Manuf Technol 2019;103(1):367–76. https://doi.org/10.1007/s00170-019-03560-1.

[40] Horstman Rt, Lieb Kc, Meltzer Rl, Moore Ic, Server WL. Impact three-point bend testing for notched and precracked specimens. J Test Eval 1978;6:29–34. https://doi.org/10.1520/JTE10915J.

[41] Kaspar R, Faul H. Charpy V subsize specimens measurements of steel impact properties. MP Materialprüfung Jahrg 2001;43:1–2.

[42] Lucon E, Van Walle E, Fabry A, Puzzolante J-L, Verstrepen A, Vosch R, et al. Correlations between standard and miniaturised Charpy-V specimens. Belgium, http://inis.iaea.org/search/search.aspx?orig_q=RN:31045631; 1998.

[43] Chen Zhe, Colliander Magnus Hörnqvist, Sundell Gustav, Peng Ru Lin, Zhou Jinming, Johansson Sten, et al. Nano-scale characterization of white layer in broached inconel 718. Mater Sci Eng, A 2017;684(January):373–84. https://doi.org/10.1016/j.msea.2016.12.045.

[44] Wang Zemin, Guan Kai, Gao Ming, Li Xiangyou, Chen Xiaofeng, Zeng Xiaoyan. The microstructure and mechanical properties of deposited-IN718 by selective laser melting. J Alloys Compd 2012;513(February):518–23. https://doi.org/10.1016/j.jallcom.2011.10.107.

[45] Fitzgerald E, Everhart W. "The effect of location on the structure and mechanical properties of selective laser melted 316L stainless steel.". Proceedings of the 27th annual international solid freeform fabrication symposium 2016 : an additive manufacturing conference 2016;574–83 [Austin, Texas, USA].

[46] Yakout Mostafa, Elbestawi MA, Veldhuis Stephen C. On the characterization of stainless steel 316L parts produced by selective laser melting. Int J Adv Des Manuf Technol 2018;95(5):1953–74.

[47] Jiang Runbo, Mostafaei Amir, Joseph Pauza, Kantzos Christopher, Rollett Anthony D. Varied heat treatments and properties of laser powder bed printed inconel 718. Mater Sci Eng, A 2019;755(May):170–80. https://doi.org/10.1016/j.msea.2019.03.103.

[48] Holland Sharniece, Wang Xiaoqing, Jia Chen, Cai Wenjun, Yan Feng, Lin Li. Multiscale characterization of microstructures and mechanical properties of inconel 718 fabricated by selective laser melting. J Alloys Compd 2019;784(May):182–94. https://doi.org/10.1016/j.jallcom.2018.12.380.

[49] Yu ZS, Zhang JX, Yuan Y, Zhou RC, Zhang HJ, Wang HZ. Microstructural evolution and mechanical properties of inconel 718 after thermal exposure. Mater Sci Eng, A 2015;634(May):55–63.

[50] Mullins MJ, Liu D, Sue H-J. Chapter 2 - mechanical properties of thermosets. In: Guo Qipeng, editor. Thermosets. second ed. Elsevier; 2018. p. 35–68. https://doi.org/10.1016/B978-0-08-101021-1.00002-2.

[51] Yu Hao, Hayashi Shigenari, Kakehi Koji, Kuo Yen-Ling. Study of formed oxides in IN718 alloy during the fabrication by selective laser melting and Electron beam melting. Metals 2019;9(1):19.

[52] Afkhami Shahriar, Dabiri Mohammad, Piili Heidi, Björk Timo. Effects of manufacturing parameters and mechanical post-processing on stainless steel 316L processed by laser powder bed fusion. Mater Sci Eng, A 2021;802(January):140660.

[53] Shrestha Rakish, Simsiriwong Jutima, Shamsaei Nima. Fatigue behavior of additive manufactured 316L stainless steel parts: effects of layer orientation and surface roughness. Addit Manuf 2019;28(August):23–38. https://doi.org/10.1016/j.addma.2019.04.011.